

Single-step additive manufacturing of silicon carbide through laser-induced phase separation

Omer Karakoc (✉ omerkarakoc2018@gmail.com)

Oak Ridge National Laboratory <https://orcid.org/0000-0001-9512-6156>

Keyou Mao

Oak Ridge National Laboratory

Jianqi Xi

University of Wisconsin-Madison

Takaaki Koyanagi

Oak Ridge National Laboratory <https://orcid.org/0000-0001-7272-4049>

Jian Liu

Polaronyx Company

Izabela Szlufarska

University of Wisconsin–Madison

Yutai Katoh

Oak Ridge National Laboratory <https://orcid.org/0000-0001-9494-5862>

Article

Keywords: additive manufacturing, femtosecond laser, silicon carbide (SiC), powder bed fusion, phase separation

Posted Date: November 9th, 2021

DOI: <https://doi.org/10.21203/rs.3.rs-1017609/v1>

License:  This work is licensed under a Creative Commons Attribution 4.0 International License.

[Read Full License](#)

Single-step additive manufacturing of silicon carbide through laser-induced phase separation

Omer Karakoc¹✉, Keyou Mao¹, Jianqi Xi², Takaaki Koyanagi¹, Jian Liu³,
Izabela Szlufarska², Yutai Katoh¹

¹ Materials Science and Technology Division, Oak Ridge National Laboratory, Oak Ridge, TN 37831, USA.

² Department of Materials Science and Engineering, University of Wisconsin-Madison, Madison, WI 53706, USA.

³ J. Liu, PolarOnyx Inc., 2526 Qume Drive, San Jose, CA 95131, USA.

✉ email: karakoco@ornl.gov

Silicon carbide (SiC) tubes are fabricated through femtosecond high-energy ultra-short pulsed laser powder bed fusion (LPBF) additive manufacturing. Widespread implementation of pulsed LPBF of SiC compounds is hampered by a poor understanding of the material–laser interaction for such short processing times and under such extreme thermal regimes, which is due to the complexity of SiC materials. In this investigation, binding and phase separation mechanisms of SiC powders driven by pulsed laser–material interactions are elucidated using numerous state-of-the-art analytical tools as well as theoretical calculations. Partial disintegration of 6H-SiC powders into silicon and carbon during laser sintering is demonstrated to bind SiC powder particles together with no measurable SiO₂ phase formation. During femtosecond laser–material interactions, 6H-SiC decomposes into silicon and carbon at high temperatures and localized high pressure state on the process. Decomposition of 6H-SiC is corroborated by density functional theory (DFT) calculations. Furthermore, relatively large (~200 nm–1.5 μm) pockets of 6H-SiC, 3C-SiC, repetitive nanoscale-pattern “nanobreathing” (~2–20 nm) of 6H-SiC and highly oriented pyrolytic graphite spheres are formed. The experimental observations indicate the viability of the synthesis of highly oriented spheroidal pyrolytic graphite and 3C-SiC and 6H-SiC grains, and thin elements of silicon and carbon, using high energy short-pulse laser irradiation.

This manuscript has been authored by UT-Battelle, LLC, under contract DE-AC05-00OR22725 with the US Department of Energy (DOE). The US government retains and the publisher, by accepting the article for publication, acknowledges that the US government retains a nonexclusive, paid-up, irrevocable, worldwide license to publish or reproduce the published form of this manuscript, or allow others to do so, for US government purposes. DOE will provide public access to these results of federally sponsored research in accordance with the DOE Public Access Plan (<http://energy.gov/downloads/doe-public-access-plan>).

Keywords: additive manufacturing, femtosecond laser, silicon carbide (SiC), powder bed fusion, phase separation

Introduction

Silicon carbide (SiC) has potential as a structural material for use in extreme environments such as space and nuclear applications owing to its strong corrosion resistance, high-temperature strength, excellent damage irradiation tolerance, adequate scattering cross-sections, and low neutron absorption^{1, 2, 3, 4}. Unlike metals or alloys^{5, 6}, however, machining, near net shaping of SiC via- conventional machining are impractical and extremely difficult due to their brittleness and chemical stability^{7, 8, 9}. Conventional machining consumes large amount of energy to shape SiC due to high sintering temperatures above 2000 °C⁹. Additive manufacturing (AM) promises a cost- and energy-effective approach to solving these issues and is a strategy for developing next-generation parts for advanced nuclear applications⁷, because it significantly reduces the amount of waste produced in the process¹⁰ and enables rapid prototyping and fabrication of parts with complex geometries. Thus, additive manufacturing of SiC is fast-growing technology for wide variety of applications¹¹.

AM technology of SiC will be revolutionary, but dense and high purity SiC part by AM have not been realized due to strong covalent nature of SiC, SiC sublimation rather than melting at high temperatures⁷. Full capability of SiC component is only achievable with nuclear-grade SiC, which is highly crystalline and dense and pure¹². AM of SiC generally involves preforming a green body and densification step⁷. Most widely used processing options for AM of SiC are wet processing (sterolithography, gel casting, and direct ink writing) and dry processing (SLS, laminated object manufacturing, and binder jet printing)⁷. Another AM process is laser-induced chemical vapor

deposition (LCVD), which uses reagent gases¹³. Heat of focused laser results in decomposition of reagent gases in which AM part is produced. Technological challenges lie in SiC densification process: part size for LCVD; high densification temperature for liquid-phase sintering; and volume shrinkage for powder sintering and pre-ceramic polymer pyrolysis⁷. AM of SiC by SLS involves reaction sintering of silicon and carbon, which results in formation SiO₂ impurities⁷.

Therefore, in the present study, single-step additive manufacturing of SiC has been developed using laser powder bed fusion (LPBF) without use of any sintering additives. Pulsed-LPBF joins materials by consolidating successive layers of powder and selectively sintering them using a high-energy pulsed laser to fabricate final components from 3D model data^{14, 15, 16}. Thus, it is possible to make objects with arbitrary geometries without the need to adapt the conventional production process itself. This approach enables LPBF to fabricate complex 3D parts with high accuracy without extensive tooling and without the geometric limitations inherent in typical subtractive manufacturing processes^{17, 18}. The capability to process a wide variety of materials with a large range of mechanical and physical properties will enable a broad range of applications in the aerospace, nuclear, biology, and medical industries^{17, 18, 19, 20, 21, 22}. Despite its great advantages, concerns over AM object quality and consistency limit the widespread utilization of LPBF²³. Large differences in the mechanical properties of AM objects pose challenges for certification authorities²⁴ and designers^{25, 26}. Sintering involves neck formation between adjacent powders to lower the free energy while powder particles grow. These regions can occur many times in a single AM part—typically close to the fusion of powder particles, where the influences on chemical, mechanical, and physical properties are the most pronounced. Thus, providing insight on the laser–matter interaction process in those regions could lead to remarkable outcomes for the quality and consistency of SiC parts fabricated by AM²⁷.

Nonetheless, there has not been extensive research to obtain significant surface information such as the microstructural evolution and binding mechanisms of single SiC powder particles under high-energy short-pulse laser irradiation. We conducted detailed microstructural characterization, which led to findings that explains the physical process of SiC AM and important laser-material interactions. Those topics are ideal for investigation by transmission electron microscopy (TEM), transmission Kikuchi diffraction (TKD), Raman spectroscopy, and scanning electron microscopy (SEM). In this study, XRD, TEM, TKD, SEM, and Raman spectroscopy are carried out to explore fiber laser–SiC powder particle interactions during AM processing and elucidate the binding mechanisms that result in the consolidation of SiC powders. Complementary microstructural characterization enables a deeper understanding of general trends in laser-SiC powder interactions and elucidates the binding mechanism and phase separations detailed in the experimental efforts. A successful mitigation has been implemented to consolidate SiC powders through phase separation of SiC (**Fig. 1**). The experimental observations, demonstrated herein, significantly improves the reliability of parts made by LPBF. Our work will lead to AM of SiC of unprecedented quality/performance and application of LPBF to refractory ceramics that are difficult to sinter. Also, this technique is very crucial for advances in the fabrication of SiC-based materials for various structural/thermal/medical applications and the semiconductor industry.

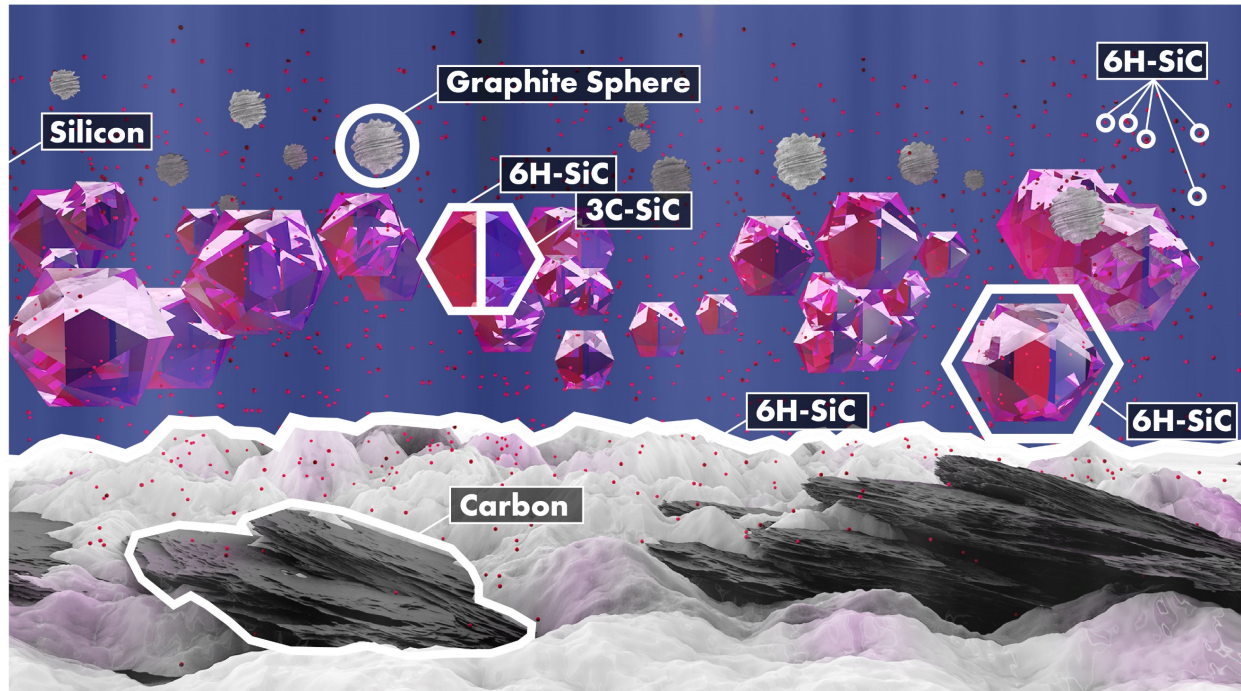


Fig. 1. Schematic illustration of phase separation of 6H-SiC particles into multiple phases and formation of 6H-SiC nanoprecipitates, spheroidal graphite, and small pockets of 3C-SiC and 6H-SiC following short pulse high energy laser-irradiation.

Results

Additive manufacturing of silicon carbide by LPBF. High-energy, short-pulse femtosecond fiber laser²⁸ (Supplementary Fig. 1) is used to fabricate dimensionally accurate SiC components from computer-aided designs (Supplementary Fig. 2). The starting SiC powders consisted of polycrystalline 6H-SiC with particle sizes of 20–40 μm and 99% nominal purity, confirmed by x-ray diffraction (XRD) patterns and Raman spectroscopy (Fig. 2). To identify the appropriate processing parameter set, various laser powers and scan speeds were applied to produce 12 SiC tubes (Supplementary Table 1). The laser-sintered compounds were viewed by SEM to assess the material structure and porosity level (Supplementary Fig. 2). As seen in Supplementary Fig. 2, the high-power femtosecond fiber laser fuses SiC powders. The structures of the top and surfaces of sintered objects appear very similar. Thus, one SEM image was selected to represent the surface

structures of the others. This approach was extended to other figures throughout the paper. The AM objects had a high level of porosity in a random pattern. Buoyancy and caliber methods were applied to measure the porosity and density of laser-sintered objects. The investigated AM objects indicated porosities from 49.8% to 53.2% (Supplementary Table 2). The AM objects investigated in this study had bulk densities from 1.50 g/cm³ to 1.61 g/cm³. All density measurements were performed based on the theoretical density of SiC, 3.21 g/cm³, which was assumed in deriving the porosity. To evaluate the effect of laser power and scanning speed, these two parameters were varied and were found to have insignificant effects on the porosity level and density of AM objects implying that the different processing parameters used in the LPBF process likely induced the same effects on the powder surface. Porosity content was ascribed to incomplete sintering in the powder layer.

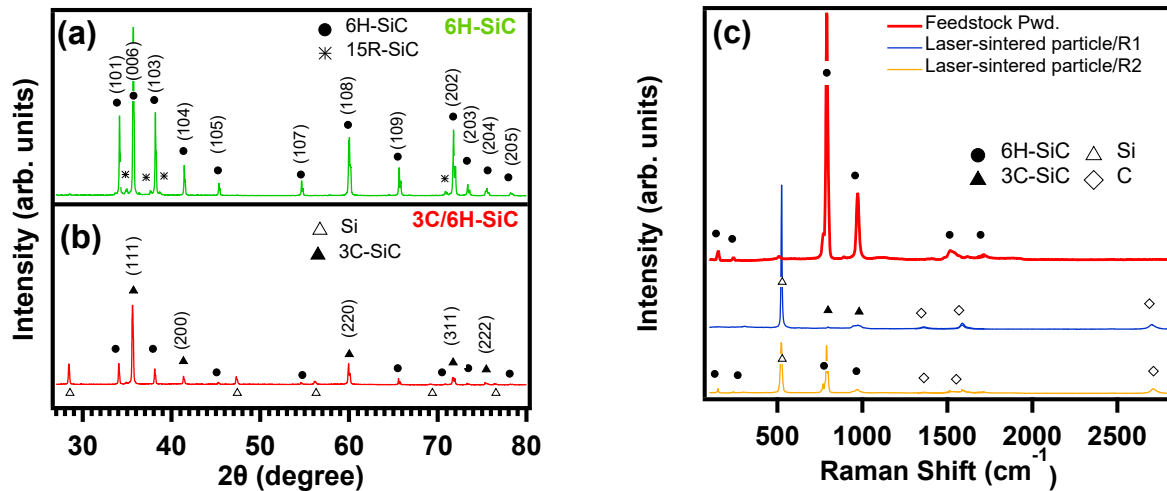


Fig. 2. Powder x-ray diffraction pattern of **a** feedstock SiC powder and **b** laser-sintered SiC. **c** Powder Raman spectroscopy of feedstock SiC and laser-sintered SiC. Four phases—6H-SiC, 3C-SiC, silicon, and carbon—were identified, as marked by symbols. The probe size of the laser was between 500 nm and 1 μ m. One representative spectra are shown for laser-sintered to demonstrate characteristic peaks of 3C-SiC and 6H-SiC found separately at two different R1 and R2 regions.

Thermal decomposition of 6H-SiC into Si and C and subsequent nucleation of different SiC polytypes and pyrolytic graphite spheres. First, two kinds of characterization tools, XRD and

Raman spectroscopy, were utilized for the phase analysis. XRD provides structural analysis—information regarding how atoms of molecules are packed in the crystalline structure—while Raman analysis is designed to examine thin structure electronic levels and vibrational modes present in a sample. Hence, the combination of XRD and Raman provided complete information regarding the structural aspects of the samples. The analysis allowed us to identify the phase separation of 6H-SiC into silicon (Si) and carbon (C) and the subsequent nucleation of 3C-SiC and spheroidal graphite (Fig. 2). XRD measurements determined structural changes and phase separation following laser irradiation (Fig. 2a, b). The as-received SiC powders were mainly identified as hexagonal 6H-SiC crystal structures and much smaller phase fractions of rhombohedral 15R-SiC. There was no detectable Si phase and SiO₂ (Fig. 2a). In addition to 6H-SiC peaks, coinciding cubic 3C-SiC and Si diffraction peaks emerged for powders obtained from laser-sintered objects (Fig. 2b). XRD results were the first experimental evidence of phase separation during laser–material interaction.

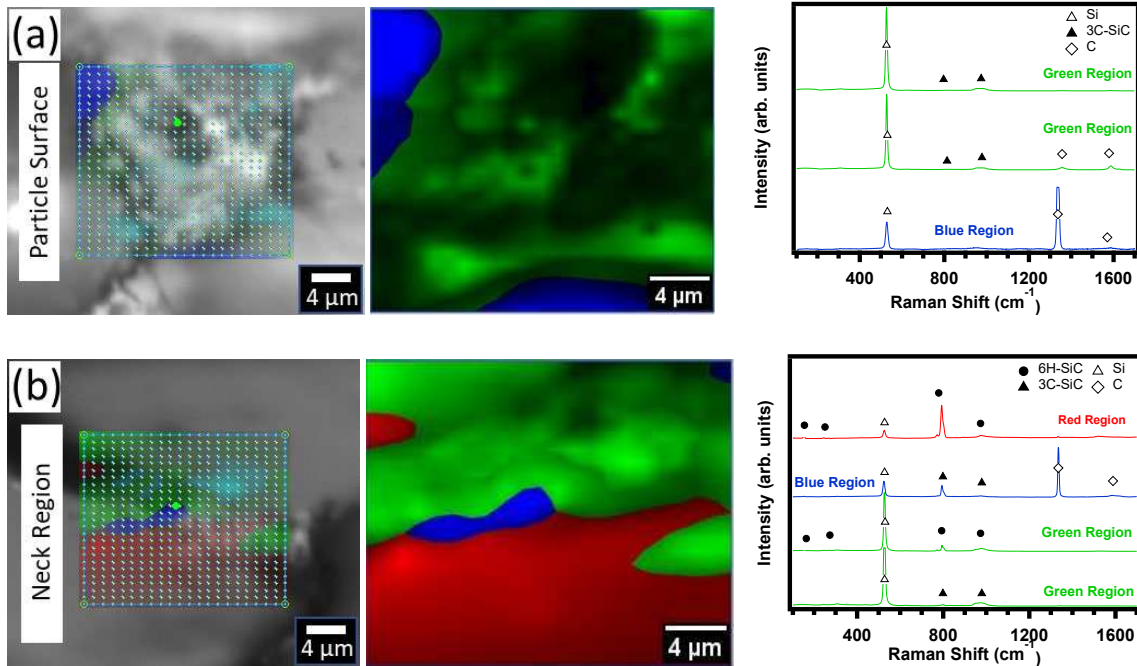


Fig. 3. Raman mapping of additively manufactured SiC part showing phase separation induced by high-energy short-pulse laser irradiation. The Raman scanner is capable of carrying out rapid point-to-point mapping of **a** the laser-irradiated particle surface and **b** the polished cross-section of the neck region where particles bind. For the area shown by each color, the corresponding Raman spectrum is demonstrated. Univariate images were constructed by bracketing bands of ~ 520 , 780 , and 1350 cm^{-1} with cursors for Si, SiC, and C, respectively. The intensity between those cursors at each data point is demonstrated in the Raman map.

Raman spectroscopy measurements were carried out on as-fabricated SiC powder and laser-sintered particles (Table S1) at various locations (Fig. 2c). The spectral range was recorded between 200 and 2800 cm^{-1} with a spectral resolution of $500\text{ nm}-1\text{ }\mu\text{m}$ and an excitation wavelength of 532 nm . As indicated in Fig. 2c, multiple peaks were identified for as-fabricated SiC powders associated with 6H-SiC. Characteristic peaks of 6H-SiC appear at 965 cm^{-1} which are associated with the LO (longitudinal) phonon mode with A_1 symmetry, at about 766 cm^{-1} and 788 cm^{-1} associated with TO (transverse) phonon modes with E_2 symmetry, and at about 240 cm^{-1} and 265 cm^{-1} associated with the E_1 and E_2 planar acoustic modes, respectively. The blue Raman spectra associated with laser-sintered parts indicate graphite with a strong intensity of the G peak at 1580 cm^{-1} . The D band at 1350 cm^{-1} shows graphite in the presence of some disorder. Carbon exhibits Raman peaks at 1350 D band , and $1580\text{ G band cm}^{-1}$ corresponding to the A_{1g} and E_{2g} modes, respectively^{29, 30, 31}. Characteristic Raman peak of silicon occurs at around 520 cm^{-1} associated with the LO phonon vibrations of the Si-Si bond³². Characteristic peaks of Si and C are absent in the Raman spectra of the as-fabricated SiC powders, hinting that the as-fabricated SiC powders consist mainly of 6H-SiC. In contrast, the Raman spectra of the laser-sintered particles are indicative of 3C-SiC, Si and C, and 6H-SiC. That result suggests that 6H-SiC decomposes into Si and C, and subsequently Si and C react to form incipient 3C-SiC, 6H-SiC during the solidification of liquid Si.

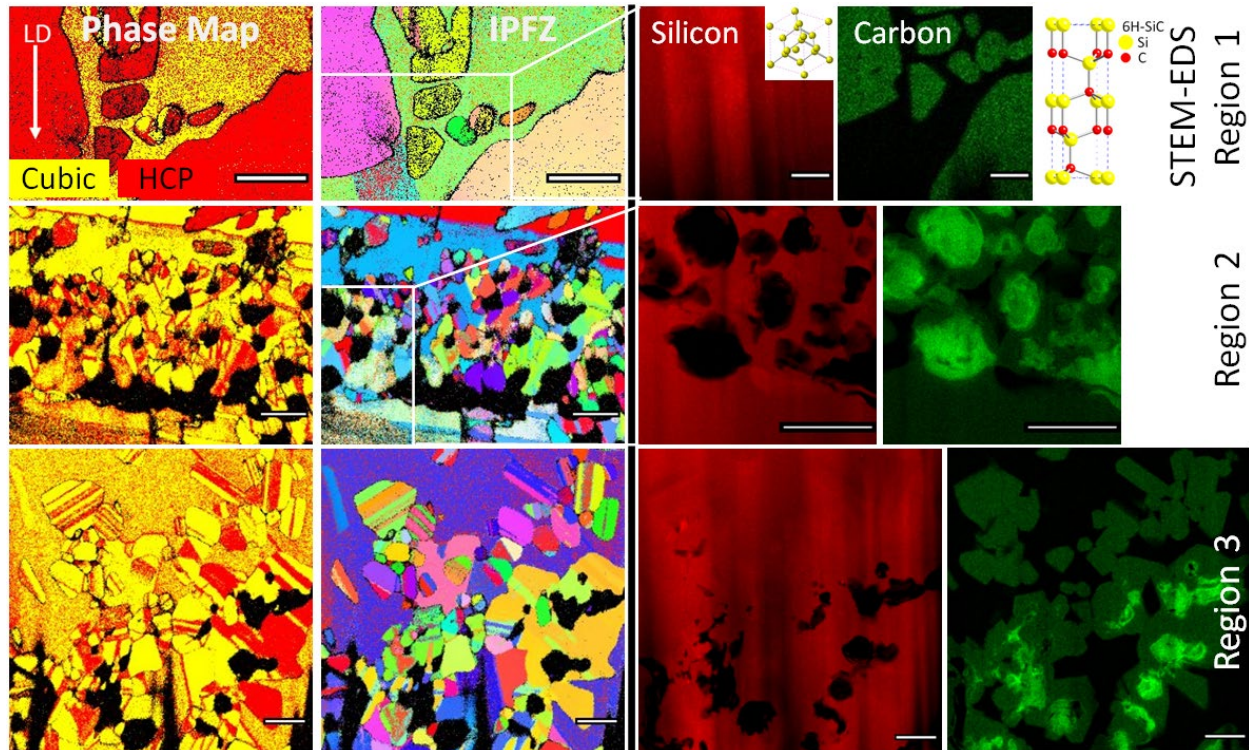


Fig. 4. SEM-TKD analysis of additively manufactured SiC parts in the region where particles join. The phase map and the inverse pole figure Z (IPFZ) of three different regions with the corresponding TEM-EDS mapping analysis of silicon, carbon is displayed. The XY -plane of images is parallel to the laser beam direction. Scale bars represent $1\ \mu\text{m}$. LD: laser direction. In the phase map, yellow areas correspond cubic crystal structure, while red areas are identified as hexagonal crystal structure. Cubic and HCP crystal structure in the phase map are yellow and red in the background, respectively. The white boxes indicate the zoomed-in areas of the STEM-EDS maps.

Raman mapping was performed on a polished cross-section of the neck region, where fusion of SiC particles occurred and SiC particles surfaced, to understand phase separation and the probability of potent nucleant particles during solidification (Fig. 3). Raman maps were acquired by moving the stage in $1\ \mu\text{m}$ increments over areas of approximately $21 \times 24\ \mu\text{m}^2$ and $22 \times 27\ \mu\text{m}^2$. A univariate image was rendered using green brackets to enclose the area around $520\ \text{cm}^{-1}$, red brackets around the area between 766 and $788\ \text{cm}^{-1}$, and blue brackets to enclose the area around $1350\ \text{cm}^{-1}$. The intensity between the bands selected by the cursors at each data point was calculated to construct the Raman image. Thus, the green, red, and blue areas in the Raman image

predominantly correspond to Si, 6H-SiC, and C, respectively. Fig. 3a demonstrates a laser-irradiated particle surface. Phase separation is clearly distinguishable on the particle surface. The green and blue areas in the Raman image are associated with strong Si and C Raman peaks, respectively. At some locations, the nucleation of the 3C-SiC polytype occurred primarily subsequent to the thermal decomposition of SiC. In Fig. 3b, Raman spectra in the red color area indicate unirradiated 6H-SiC powder with an accompanying intensity peak at 520 cm^{-1} that is the characteristic peak of Si. The Raman scattering efficiency of crystalline Si is about ten times greater than that of the crystalline SiC peaks^{31, 33}. Thus, Si content is negligible in the red area. The blue area predominantly consists of C and small amounts of 3C-SiC and Si. The green area is indicated by two separate Raman spectra. In addition to a Si signal at around 520 cm^{-1} , one spectrum has the characteristic peak of 3C-SiC and the second contains the Raman spectrum of 6H-SiC. The important takeaway point from the Raman data is that following the laser-driven solid-state phase separation of 6H-SiC, the solidification process favored the reaction of Si and C to form 3C-SiC and 6H-SiC, depending on the equilibrium conditions and temperature.

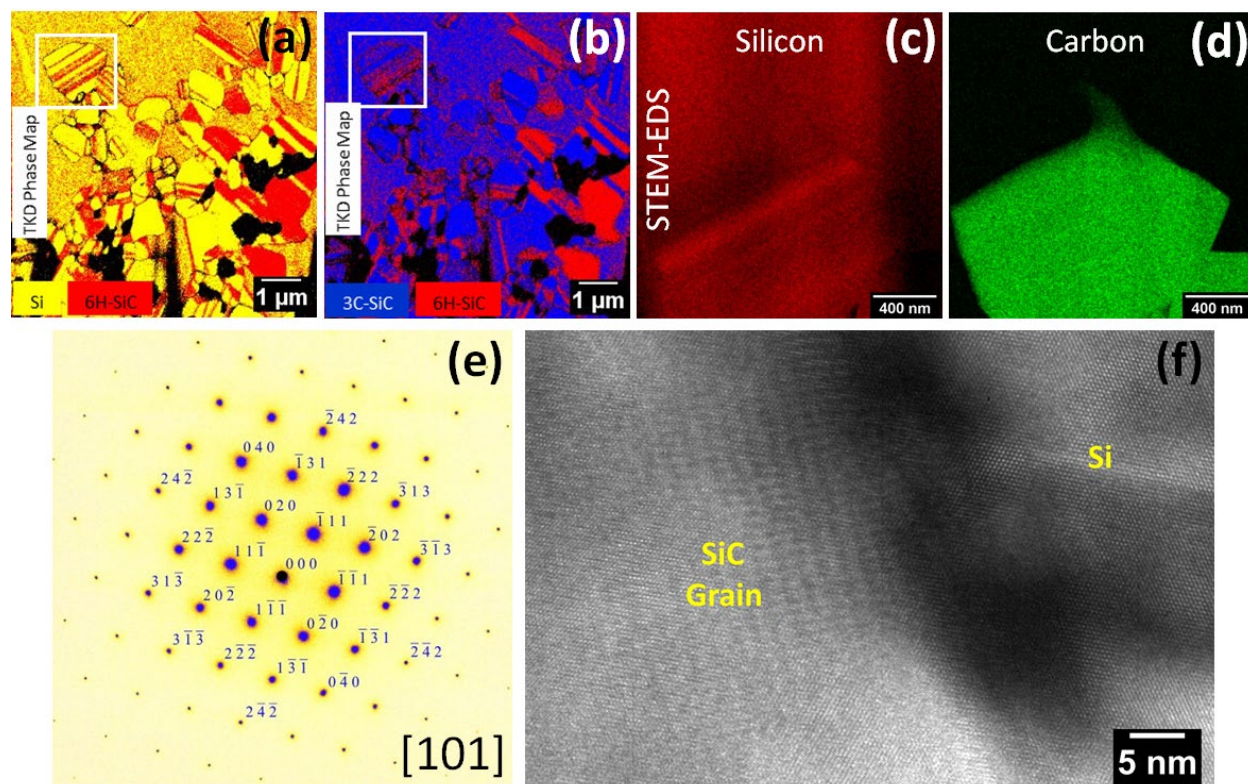


Fig. 5. TKD phase mapping performed with a combination of Si/6H-SiC and 3C-SiC/6H-SiC. **a** The yellow-colored area (cubic-Si phase) turns into **b** a blue-colored area (cubic-3C-SiC) when silicon is removed from the TKD analysis. **c** TEM-EDS mapping was performed at the interface of one selected grain indicated by white box for silicon and **d** carbon. **e** Selected area diffraction pattern (SADP) and **f** HRTEM images were captured on the [101] zone axis at the interface of the selected grain. The lattice spacing of the 3C-SiC inside grain is smaller than the encapsulating silicon phase, indicating two different phases identified as the same during TKD analysis.

Further characterizations were performed via SEM, TKD, STEM, and HRTEM to provide insight into the occurrence of phase separation and the nucleation of 3C-SiC, 6H-SiC polytypes, and graphite. The microstructural features after laser sintering were investigated to assess the binding mechanism and phases at junctions using backscattered-electron (BSE) imaging and energy-dispersive x-ray spectroscopy (EDS) elemental distribution mapping. Supplementary Fig. 3 indicates a mirror-polished cross-section of a laser-sintered part. The presence of different phases is clearly distinguishable, particularly at the locations where particles bind. Further composition analysis using SEM-EDS maps of elemental distribution illustrates the C and Si variation across

the polished cross-section of the AM object (magnified in Supplementary Fig. 3b, c). It reveals that Si is enriched at the particle-particle interface, where C is depleted. The high-intensity red area is a consequence of using a C polymer during the polishing of the AM parts. Silicon enrichment at some locations was ascribed to laser-heating-induced SiC decomposition. The elemental distribution map revealed that a Si-rich phase played a significant role in the fusion of 6H-SiC powder particles. These regions occurred thousands of times throughout the laser-sintered parts and consolidated the SiC tubes.

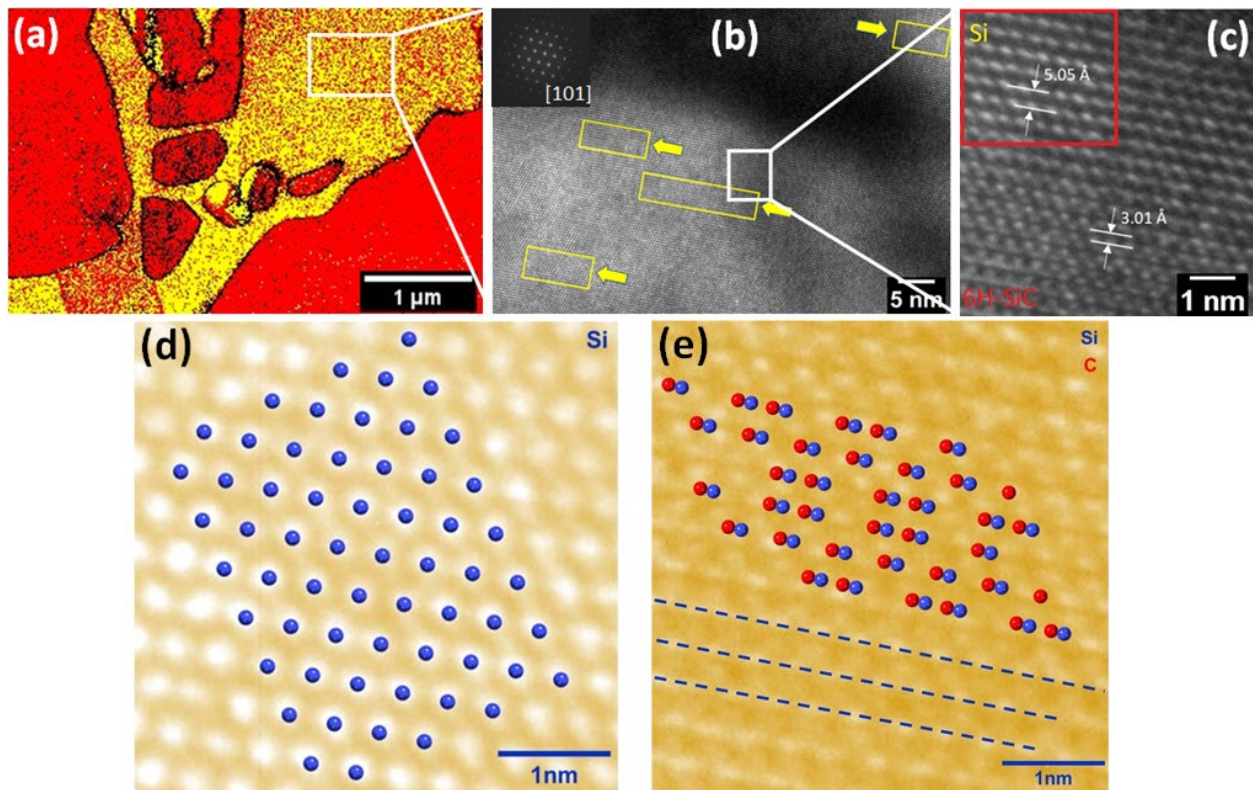


Fig. 6. **a** TKD phase map showing 6H-SiC nanoprecipitates “nanobreathing,” uniformly dispersed in the silicon phase, and **b** HRTEM images captured from the white panel in the TKD map on the [101] zone axis **c** magnified HRTEM image marked by white box. Boxes marked by yellow arrows indicate the formation of 6H-SiC nanoprecipitates in silicon, as distinguished by differences in lattice spacing; silicon: 5.05 Å, 6H-SiC: 3.01 Å *a*-direction. **d** Simulated BF-HRTEM patterns of silicon and **e** 6H-SiC. Silicon and 6H-SiC are on the [101], [10 $\bar{1}$ 0] zone axis, respectively.

To obtain a better understanding of the underlying mechanism that governs phase separation and fusion of SiC particles, three TEM lamellas were prepared from three different locations where two SiC particles bind together and the Si phase exists as an interface (Supplementary Fig. 3). Fig. 4 demonstrates the results of TKD mapping and corresponding STEM-EDS analysis. The images at the top, middle and bottom in Fig. 4 represent region 1, 2 and 3, respectively. The XY-plane refers to the layer that is fabricated parallel to the building direction in the laser sintering process. Identification of cubic and hexagonal crystal structures and undetected region was carried out through TKD mapping, and spatial distribution mapping of Si and C was performed by STEM-EDS. The combination of TKD mapping and STEM-EDS enabled precise phase identification during laser-material interactions. The phase separation at the irradiated area is clearly distinguishable. Region 1 indicates that the reaction layer is composed of two crystal structure, cubic and hexagonal. The phase map exhibits the cubic phase connecting two hexagonal powders. Moreover, relatively large pockets of hexagonal phase grains are dispersed inside the cubic phase, with grain sizes ranging from 500 nm to 1.5 μm . The TKD phase map of region 2 and 3 shows that the reaction layer consists of cubic, hexagonal nano-precipitates and some undetected areas.

To resolve the undetected region, a corresponding STEM-EDS analysis was performed in the same region where the TKD mapping was obtained. The intensity of silicon phase is relatively uniform across region 1, while carbon is depleted in some parts of the region investigated where two SiC powders are apparently joined by a cubic phase but is enriched in the relatively large pockets of hexagonal phase inside the Si interface and hexagonal powders. STEM-EDS analysis of region 2 and 3 indicated that areas undetected by TKD mapping were C phase. In the C-rich region, there is a lack of Si content. The analysis showed this region almost completely took the

form of C. TKD mapping is unable to differentiate the cubic Si and 3C-SiC due to similarity in Kikuchi pattern of these phases, while hexagonal phase is identified as 6H-SiC.

To differentiate cubic phases and provide understanding of the structural order of the C phase, TEM analysis was performed in the modes of STEM, HRTEM, and bright-field TEM (BFTEM). Fig. 5a, b indicate TKD mapping in the presence of a cubic Si phase and 3C-SiC, respectively. The yellow region assigned to the Si phase transformed into 3C-SiC once it was removed from the TKD mapping. The underlying reason behind the overlapping of two phases was that both the 3C-SiC and the Si phase contained a cubic structure, and the Kikuchi patterns are quite similar. TKD mapping was unable to distinguish cubic Si and 3C-SiC simultaneously. Thus, all cubic phases are identified as either Si or 3C-SiC. High-magnification STEM-EDS was performed in the yellow area (marked with a white box) where one grain was surrounded by another phase (Fig. 5c, d). The Si distribution was relatively uniform. Unlike the Si distribution, C was enriched in the grain but absent in the surrounding area encapsulating the grain. This observation hints that the yellow area in the grain might be 3C-SiC while the surrounding grains are the Si phase. To provide additional evidence for this hypothesis, as indicated in Fig. 5e, f, HRTEM analysis was performed on the [101] zone axis at the intersection of the grain and the Si phase marked by white box in the Fig. 5a, b. The lattice spacing of Si and 3C-SiC was 5.10 Å (real lattice spacing [RLS] ~5.43 Å) and 4.10 Å (RLS ~ 4.35 Å), respectively³⁴. The HRTEM images indicate different lattice spacings inside and outside the grains. A larger lattice distance is associated with the Si phase and the smaller lattice spacing in the grain corresponds to 3C-SiC. This observation reconciled the results of the TKD mapping with the XRD and Raman analyses.

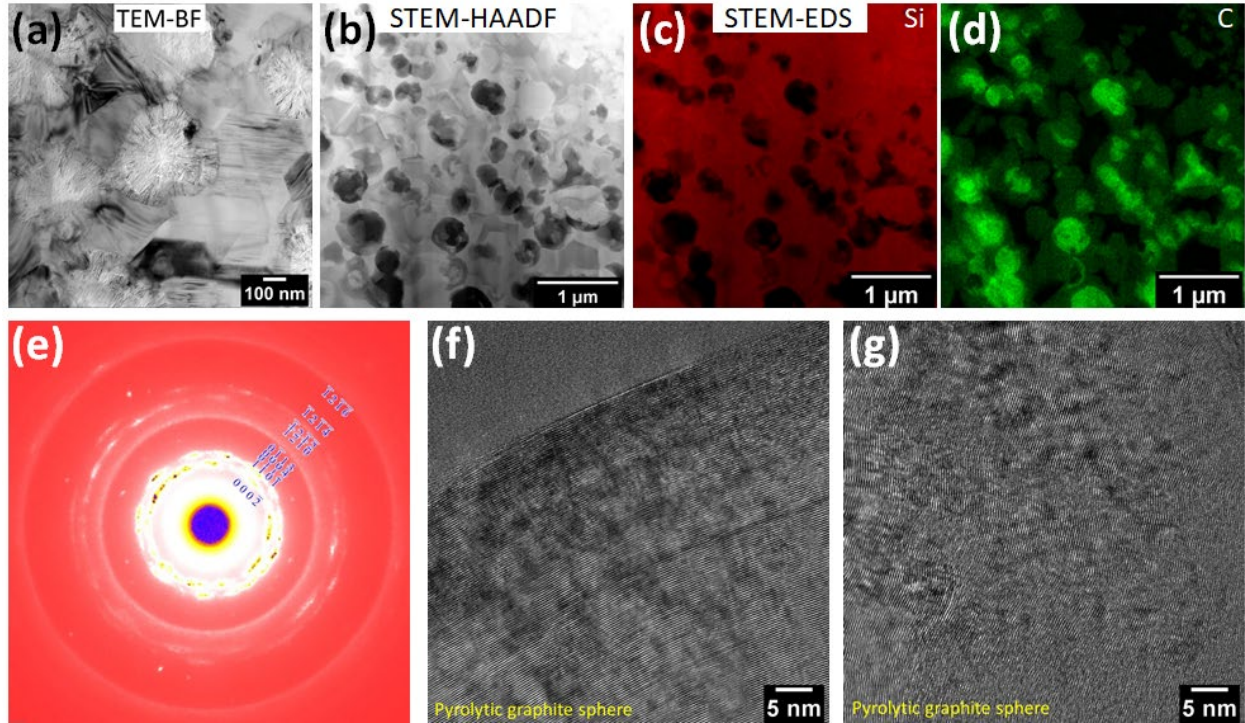


Fig. 7. Detailed examination of formation of pyrolytic graphite sphere (PGS) during laser-material interaction. **a** bright field (BF) TEM **b** STEM-HAADF images showing dispersion of spheroidal graphite. **c** STEM-EDS analysis of STEM-HAADF image with element mapping of silicon and **d** carbon. **e** SADP of graphite captured from PGS, **f** HRTEM images showing highly oriented graphite on near periphery and **g** relatively less ordered graphite in near central region.

Our results also indicated that the 6H-SiC nano-precipitates was formed on the order of $\sim 2\text{--}20$ nm. We called these repetitive nanoscale 6H-SiC patterns “nanobreathing”. The TKD phase map shown in Fig. 6a clearly demonstrates red dots (6H-SiC) in the yellow region (Si). Detailed examination of these small features was performed using HRTEM inside the cubic Si phase on the [101] zone axis (Fig. 6b, c). The TKD phase map exhibits densely populated, uniformly dispersed nanoscale 6H-SiC precipitates inside the cubic Si. The distribution of these nanoscale patterns appears homogenous across the Si phase. The white box in the TKD phase map denotes where HRTEM was performed. The 6H-SiC nanoprecipitates in the [101] zone are marked with arrows

to indicate the difference in lattice spacing between Si and the incipient of 6H-SiC (Fig. 6c). The lattice spacing in the Si and 6H-SiC *a*-direction was 5.10 Å (RLS ~5.43 Å) and 3.01 Å (RLS ~3.08 Å), respectively, which was near the Si and 6H-SiC *a*-direction lattice parameter³⁴. Based on SADPs, simulated crystal models are constructed using CrystalMaker®, as overlays on the HRTEM images of silicon and 6H-SiC for better understanding (Fig. 6d, e).

Carbon can exist in various forms. Fig. 7 indicates selected area diffraction pattern (SADP) results for graphite taken from pyrolytic graphite spheres (PGSs), STEM-high-angle annular dark-field (HAADF), BFTEM, HRTEM, and corresponding STEM-EDS of the STEM-HAADF images. Femtosecond laser irradiation resulted in the formation of well-ordered and highly oriented PGSs through a solid-solid transformation (Fig. 7e, f, g). The diameter span range was 200–600 nm. The HRTEM images show the graphitic degree of the C materials. The interplanar spacing near the periphery of the PGSs is about 3.43 Å. The fringes in each sector near the periphery are mostly parallel straight lines, exhibiting a high graphitic degree. The PGSs were found to disperse nonuniformly in the region where the phase separation of SiC took place (Fig. 7a, b). In the STEM-HAADF images, the brightest areas correspond to heavy Si atoms and the darkest areas represent light C atoms. The contrast of the SiC grains is between Si and C. The TEM-BF images indicate that the shapes, morphology, and structural order of the PGSs are quite similar (Fig. 7a). HRTEM images indicate that the peripheries of the PGS exhibit a higher degree of graphitization than the central regions (Fig. 7f, g). The STEM-EDS results were highly consistent with the STEM-HAADF analysis (Fig. 7c, d). Silicon is absent, whereas C is enriched, which is sign of PGS formation. These results confirmed the graphite synthesis whose characteristic peaks were also detected through Raman analysis. Even though pyrolytic graphite is commonly obtained through gas-solid

transformations like chemical vapor deposition, this study proves that laser-induced solid-state disintegration of SiC can also be used to synthesize spheroidal pyrolytic graphite. Fig. 1 schematically illustrates the laser-induced phase separation of 6H-SiC into Si and C and subsequent formation 6H-SiC nanoprecipitates, spheroidal graphite and small pockets of 3C- and 6H-SiC.

Discussion

In this study, single-step AM of SiC via powder sintering routes is demonstrated, followed by extensive microstructural characterization. Fabrication of AM SiC was achieved without the use of sintering additives or binder elements. In addition, undesired SiO₂ formation was not observed during the laser-material interactions (Fig. 2). The mechanism responsible for consolidation of SiC powders may lie in inertial confinement fusion. Very short pulse and high power laser may result in highly localized high pressure state on the process. Thus, highly volatile Si reacts with carbon rather escaping under vacuum environment due to laser confinement. Juodkazis et al. showed formation of nano-cavities in sapphire by single, 800 nm, 150 fs, 120 nJ pulses³⁵. Single laser pulse (100 nJ, 800 nm, 200 fs) produced high temperature (5×10^5 K) and pressure (~ 10 TPa)³⁵. This study supports the possibility of high pressure state during material-laser interaction.

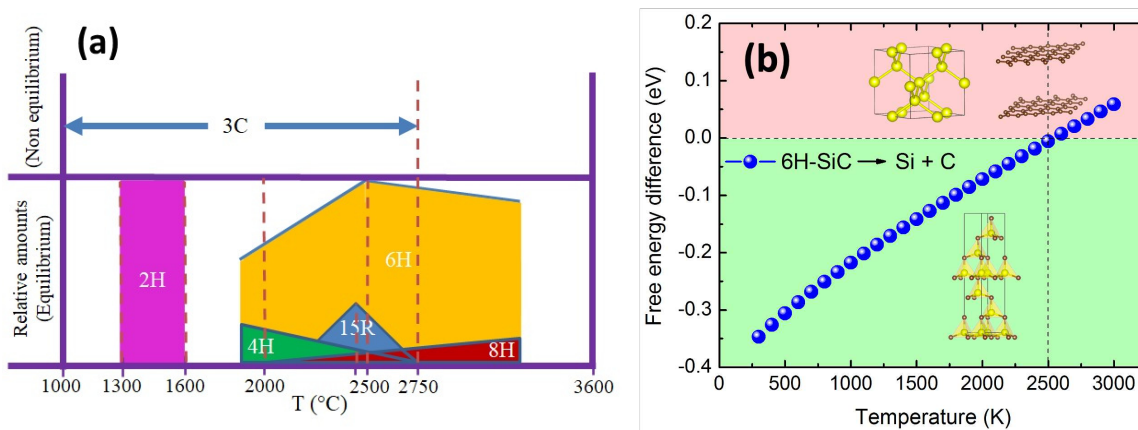


Fig. 8. a Temperature dependence of stability diagram for many different SiC polytypes³⁶. **b** Temperature dependence of the decomposition free energy for the reaction of $6\text{H-SiC} \rightarrow \text{Si} + \text{C}$ at 1 atm. The decomposition reaction occurs when the free energy become positive above ~ 2500 K.

There was a narrow process window that was satisfactory for the fabrication of SiC tubes as designed⁷. In this narrow gap, varying AM parameter sets, such as laser powers and scanning speeds, had insignificant impacts on the properties of the AM parts. Tubes made with different parameters sets were consolidated. Density measurements revealed almost equivalent porosity levels and densities for all AM parts. This equivalence can be ascribed to sufficient laser energy and scanning speed delivered to the powder bed to bind the SiC powder particles via the disintegration of SiC. The laser is only connecting the neighboring powder particles without much changing the particle shapes and how the particle are stack together. There is very little or no displacement of particles.

To adequately reveal the nucleation mechanism of the 6H and 3C polytypes after the decomposition of SiC, we referred to the literature on polytypes and the thermodynamic stability of SiC. Some previous studies reported that 4H-SiC and 6H-SiC are the most stable polytypes while 3C-SiC is the most open and least stable polytype at any temperature^{37, 38, 39, 40}. Our experimental observations were inconsistent with those predictions regarding the free energy of SiC polytypes, because our XRD and Raman analysis indicated that 3C-SiC grew in preference to all other polytypes and nucleation of hexagonal 6H-SiC occurred less frequently. In nonequilibrium conditions (high supersaturation), cubic 3C-SiC may initially form in growth experiments over the broad temperature range of $1000\text{--}2750$ °C (Fig. 8a)^{36, 37}. The high-energy short-pulse femtosecond laser fiber induced high nonequilibrium cooling conditions, which yielded a rich variety of microstructures and often preferentially selected nonequilibrium growth

modes (Fig. 3) ⁴¹. Thus, the present study results are highly consistent with the phase stability diagram of SiC (Fig. 8a) ³⁶. Small quantities of impurities and non-stoichiometry also had a great impact on polytype stabilization. The partial pressure of Si vapor was several times higher than that found in C ⁴². The multiplicity of low-energy surfaces and the high-symmetry nature of 3C-SiC may account for its occurrence in the initial stages of growth over a broad range of temperature (1400–2000 °C). These factors could have given rise to rapid growth and easy nucleation along several directions, which led to large crystals bounded by low-energy forms ³⁷. While this kinetic argument can be linked to the occurrence of 3C-SiC over a large temperature range, its high symmetry presumably increased the vibrational entropy contribution to the free energy, hence making a contribution to the equilibrium stability of 3C-SiC at elevated temperatures. Besides that, the temperature-dependent free reaction energy for the decomposition reaction of 6H-SiC \rightarrow Si + C has been calculated through the density functional theory (DFT), as shown in Fig. 8b. The positive free reaction energy means that the decomposition reaction is energetically favorable. From Fig. 8b, we can see that the decomposition reaction occurs above \sim 2500 K. This is consistent with the previous experiments, in which the decomposition of SiC into solid C plus liquid Si begins at \sim 2840 K ⁴³. The slight difference of the DFT results with the experimental value could arise from the approximation of the anharmonic effect at high temperatures.

This study establishes a fundamental understanding of the phase separation mechanism of a complex SiC compound material during high-energy short-pulse laser–material interactions. Extensive microstructural observation by XRD, Raman spectroscopy, SEM, TEM, and TKD revealed the decomposition and surface reconstruction of SiC. Thus, phase separation was confirmed by multiple characterization tools. It was found that femtosecond laser irradiation

yielded a rich variety of microstructures and phases—thin Si and C nanomaterials, multiscale 6H- and 3C-SiC pockets, and highly ordered PGSs. The polytype 6H-SiC decomposed into Si and C, and subsequently $\text{Si}(l)+\text{C}(s)\rightarrow \alpha$ or β $\text{SiC}(s)$ reactions occurred to form multiscale 6H- and 3C-SiC pockets (Fig. 4). For the first time, densely populated, uniformly dispersed nanoscale ($\sim 2\text{--}20$) 6H-SiC precipitate-nanobreathing was formed inside a Si phase following the phase separation of 6H-SiC by laser irradiation. This remarkable discovery can be exploited in many different ways, particularly in semiconductor and solar cell applications. For instance, 6H-SiC nanoprecipitates can yield enhanced mechanical properties in the Si phase, and 6H-SiC nanoprecipitates can impede dislocation slips that can increase the yield strength of Si-based materials. Furthermore, optical properties of Si can be tuned in the presence of nanoscale 6H-SiC precipitates. Overall, exploiting these 6H-SiC precipitates inside Si deliberately using femtosecond laser irradiation could pave the way for new advanced material applications accompanied by better mechanical properties.

To the best of author's knowledge, for the first time, highly oriented PGSs were reported during the phase separation of SiC using high-energy laser irradiation. Fig. 7 shows the HRTEM analysis of the 002 fringes of a PGS. A high degree of graphitization occurring near the periphery of graphite sphere can be deduced from the fringes, which are mostly aligned as parallel straight lines. Elemental mapping through the cross-section of the focused ion beam foil revealed the formation of a C sphere; Si was absent when C was enriched. Spheroidal graphite was produced through solid-to-solid transformation. High-energy short-pulse laser-derived graphite aggregate tended to extend in the c -direction rather than the a -direction, generating spheroidal (nodular) graphite. Graphite spheroids are widely found in spheroidal graphite cast iron^{44, 45}. Spheroidal graphite acts as a “crack arrester” because its rounded shapes induce fewer stress points—

hindering the formation of cracks—and enable enhanced ductility and toughness. Unlike metals, Si is intrinsically brittle and not ductile. Thus, ultra-fine dispersion of nanospheroidal graphite may lead to emergent functionality of materials.

In summary, this study revealed the phase separation of SiC powders into Si and C, induced by femtosecond laser irradiation, which joined the SiC powders together to produce dimensionally accurate SiC parts. To gain insight, DFT calculation was performed for phase separation of SiC into Si and C. Our combined theoretical calculation and experimental observation demonstrated that 6H-SiC becomes energetically more favorable for decomposition above ~2500 K. For the first time, unexpected PGSs and uniformly dispersed 6H-SiC nanoprecipitate “nanobreathing” were observed experimentally in a laser-6H-SiC compound material. The introduction of these nanoprecipitates and spheroidal graphite inside Si in a controlled manner using a high-energy laser may pave the way for new structural, electronic, medical, and energy applications.

Methods

Laser powder bed fusion. Silicon carbide powders (SiC, American Elements, purity: 99 %, particle size: 20–40 μm) were used during AM. A high-power Yb-doped fiber laser (Laser-Femto Inc., San Jose, California) was employed to fabricate SiC tubes. The Yb-doped fiber laser had a central wavelength of 1030 nm, delivering up to 250 W average power at pulse repetition rate of 80 MHz. The full-width-half-maximum (FWHM) pulse width was 800 fs. Supplementary Fig. 1 is a schematic illustration of the experimental setup. Laser powers of 125 to 150 W and scan speeds of 200 and 300 mm/s were varied to evaluate their influence on the powder sintering. SiC powders were deposited to fabricate SiC tubes in an aluminum container. To prevent oxidation, the

processing chamber was filled with industrial standard Ar. Supplementary Fig. 2 indicates the printed ($1.5 \times 10 \times 10 \text{ mm}^3$) SiC tubes.

X-ray diffraction. Room-temperature powder XRD was performed on a D2 Phaser XRD diffractometer (Bruker, Germany) in the reflection mode, $\text{CuK}\alpha$ radiation with a wavelength of 1.54 \AA . Powder data were analyzed using TOPAS profile fitting-based software for microstructure analysis.

Raman Spectroscopy. The room-temperature micro-Raman scattering measurement was conducted on as-fabricated SiC powder and laser-sintered SiC components using a confocal LabRAM HR Evolution, Horiba Scientific Raman spectroscope. The Raman excitation source was a 532 nm highly monochromatic laser (2.33 eV) and 100X objective in conjunction with a volume holographic grating notch filter and laser line rejection filter. The spot size of the 532 nm laser was estimated to be between 500 nm and $1 \text{ }\mu\text{m}$ with a laser power of 2 mW. Raman images were obtained by moving the stages with a step size of $1 \text{ }\mu\text{m}$ over an area of approximately $21 \times 24 \text{ }\mu\text{m}^2$ and $22 \times 27 \text{ }\mu\text{m}^2$ at the powder neck region and powder surface, respectively. The Raman image was constructed using green-colored brackets enclosing 520 cm^{-1} , red brackets enclosing between 766 and 788 cm^{-1} , and blue brackets enclosing 1350 cm^{-1} .

SEM. Laser-sintered components were analyzed by SEM (Tescan Mira3) to gain knowledge of the porosity level and binding mechanism of the SiC powders. The cross-sectional microstructure analysis at powder neck region was carried out using BSE imaging at an accelerating voltage of 10 kV. Elemental distribution mapping was performed using EDS analysis to determine the distribution of Si and C. A thin foil with a high-quality polished surface was prepared using an FEI Quanta focused ion beam with a low accelerating voltage of 5 kV and 2 kV at the final thinning step. TKD maps was generated using an Oxford Instruments Nordlys detector mounted on a

Tescan Mira3 with an accelerating voltage of 20 kV in high current mode. TKD mapping was conducted at a working distance of about 4 mm with a tilting angle of -20° and step size of 20 nm.

TEM. Electron-transparent TEM lamella were prepared using an FEI Quanta focused ion beam at 30 kV for rough milling, and at 5 and 2 kV for final thinning. Two TEMs were applied for microscopy and analytical analysis. The structural and compositional analyses of region 1 were carried out using a JEOL JEM2100F with an accelerating voltage of 200 kV, equipped with an energy-dispersive x-ray (EDX) detector for elemental distribution mapping. HRTEM images were acquired on the [101] zone axis. TEM, STEM, and STEM-EDS of region 2 and 3 were carried out in an FEI Talos F200X with an accelerating voltage of 200 kV and a high-efficiency Super-X EDS system. An HAADF detector was used for Z-contrast imaging. Energy peaks used for EDS analysis were Si ($K\alpha=1.739$ keV), C ($K\alpha=0.277$ keV), and O ($K\alpha=0.525$ keV).

DFT calculations. For the calculation of the phase decomposition of 6H-SiC into elemental Si and C (here we use the graphite as the reference phase), we calculate the Helmholtz free energies of these materials at different temperatures. The Helmholtz free energy F for one given material is calculated as

$$F = E_0 + F_{vib} + F_A$$

where E_0 is the total energy as evaluated in the DFT calculations. F_{vib} is the vibrational contribution to the free energy ($F_{vib} = E_{vib} - TS_{vib}$). It includes vibrational energy, E_{vib} (including zero-point energy (ZPE)), and vibrational entropy, S_{vib} . Both are calculated in the harmonic approximation from the partition function of an N -atomic system⁴⁶.

$$F_{vib} = \frac{1}{2} \sum_{i=1}^{3N} \hbar\omega_i + k_B T \ln \prod_{i=1}^{3N} (1 - e^{-\hbar\omega_i/k_B T})$$

here ω_i is $3N$ vibrational modes. F_A is the anharmonic free energy. In order to estimate the anharmonic free energy, we followed the approach of Wallace⁴⁷ who showed that the anharmonic part of the free energy can be written as $F_A = A_2 T^2$. Experiments for different crystals showed that there is an empirical relation between the average Gruneisen parameter $\langle\gamma\rangle$ and A_2 , which is given per atom by $A_2 = 3k_B/\Theta_{H\infty} (0.0078\langle\gamma\rangle - 0.0154)$ ⁴⁸. The values of Gruneisen parameter for 6H-SiC, Si, and C are 1.23⁴⁹, and 2.28⁵⁰, respectively. $\Theta_{H\infty}$ is the high temperature harmonic Debye temperature defined by $\Theta_{H\infty} = \hbar(5\langle\omega^2\rangle/3)^{1/2}/k_B$ ⁴⁸. The setting of DFT calculations have been discussed elsewhere⁵¹.

Data availability

Supporting Information is available in the supplementary materials and more data can be obtained upon reasonable request from the corresponding author.

Acknowledgements

This research was sponsored by DOE Office of Fusion Energy Sciences, DE-AC05-00OR22725 and Advanced Research Projects Agency-Energy (ARPA-E) with UT-Battelle, LLC. This research was carried out using instrumentation provided by the Department of Energy, Office of Nuclear Energy and the Nuclear Science User Facilities. The author would like to thank Dr. Caleb Massey, ORNL, and Dr. Daniel Morral, ORNL for their helpful advice and ORNL LAMDA lab Radiological Control Technician for their efforts.

Author contributions

Y. K. and T.K. conceived, designed and proposed the experiment and microscopy analysis effort; O. K. conducted Raman spectroscopy, SEM, XRD, S/TEM, TKD, and drafted the manuscript; K.M. conducted STEM, EDS and helped in writing the original draft; J.L. fabricated the SiC AM

parts using femtosecond laser; J. X. and I. S. contributed to DFT calculation. All authors analyzed the results, contributed to scientific discussion, and commented on the manuscript.

Computing Interests

The authors declare no conflict of interest.

References

1. Zinkle S, Terrani K, Snead L. Motivation for utilizing new high-performance advanced materials in nuclear energy systems. *Current Opinion in Solid State and Materials Science* **20**, 401-410 (2016).
2. Roy J, Chandra S, Das S, Maitra S. Oxidation behaviour of silicon carbide-a review. *Reviews on advanced materials science* **38**, (2014).
3. Terrani KA, Pint BA, Parish CM, Silva CM, Snead LL, Katoh Y. Silicon carbide oxidation in steam up to 2 MPa. *Journal of the American Ceramic Society* **97**, 2331-2352 (2014).
4. Katoh Y, Nozawa T, Snead LL, Ozawa K, Tanigawa H. Stability of SiC and its composites at high neutron fluence. *Journal of Nuclear Materials* **417**, 400-405 (2011).
5. Hirt L, Reiser A, Spolenak R, Zambelli T. Additive manufacturing of metal structures at the micrometer scale. *Advanced Materials* **29**, 1604211 (2017).
6. Han C, Fang Q, Shi Y, Tor SB, Chua CK, Zhou K. Recent advances on high - entropy alloys for 3D printing. *Advanced Materials* **32**, 1903855 (2020).
7. Koyanagi T, Terrani K, Harrison S, Liu J, Katoh Y. Additive manufacturing of silicon carbide for nuclear applications. *Journal of Nuclear Materials* **543**, 152577 (2021).

8. Katoh Y, *et al.* Current status and critical issues for development of SiC composites for fusion applications. *Journal of Nuclear Materials* **367**, 659-671 (2007).
9. Pawar P, Ballav R, Kumar A. Machining processes of silicon carbide: a review. *Reviews on Advanced Materials Science* **51**, 62-76 (2017).
10. Mami F, Revéret JP, Fallaha S, Margni M. Evaluating eco - efficiency of 3D printing in the aeronautic industry. *Journal of Industrial Ecology* **21**, S37-S48 (2017).
11. Colorado HA, Velásquez EIG, Monteiro SN. Sustainability of additive manufacturing: the circular economy of materials and environmental perspectives. *Journal of Materials Research and Technology* **9**, 8221-8234 (2020).
12. Terrani KA. Accident tolerant fuel cladding development: Promise, status, and challenges. *Journal of Nuclear Materials* **501**, 13-30 (2018).
13. Zhang S, Tu R, Goto T. High - speed epitaxial growth of β - SiC film on Si (111) single crystal by laser chemical vapor deposition. *Journal of the American Ceramic Society* **95**, 2782-2784 (2012).
14. Tian Y, Muñoz-Lerma J, Brochu M. Nickel-based superalloy microstructure obtained by pulsed laser powder bed fusion. *Materials Characterization* **131**, 306-315 (2017).
15. Chou R, Ghosh A, Chou S, Paliwal M, Brochu M. Microstructure and mechanical properties of Al10SiMg fabricated by pulsed laser powder bed fusion. *Materials Science and Engineering: A* **689**, 53-62 (2017).
16. Karayagiz K, *et al.* Numerical and experimental analysis of heat distribution in the laser powder bed fusion of Ti-6Al-4V. *IISE Transactions* **51**, 136-152 (2019).

17. Gibson I, Rosen D, Stucker B, Khorasani M. *Additive manufacturing technologies*. Springer (2014).
18. Wong KV, Hernandez A. A review of additive manufacturing. *International scholarly research notices* **2012**, (2012).
19. Guzzi EA, Tibbitt MW. Additive manufacturing of precision biomaterials. *Advanced Materials* **32**, 1901994 (2020).
20. Chimene D, Kaunas R, Gaharwar AK. Hydrogel bioink reinforcement for additive manufacturing: a focused review of emerging strategies. *Advanced materials* **32**, 1902026 (2020).
21. Velasco - Hogan A, Xu J, Meyers MA. Additive manufacturing as a method to design and optimize bioinspired structures. *Advanced Materials* **30**, 1800940 (2018).
22. Compton BG, Lewis JA. 3D - printing of lightweight cellular composites. *Advanced materials* **26**, 5930-5935 (2014).
23. Seifi M, *et al.* Progress towards metal additive manufacturing standardization to support qualification and certification. *Jom* **69**, 439-455 (2017).
24. Roca JB, Vaishnav P, Fuchs ER, Morgan MG. Policy needed for additive manufacturing. *Nature materials* **15**, 815-818 (2016).
25. Beese AM, Carroll BE. Review of mechanical properties of Ti-6Al-4V made by laser-based additive manufacturing using powder feedstock. *Jom* **68**, 724-734 (2016).
26. Simonelli M, Tse YY, Tuck C. Effect of the build orientation on the mechanical properties and fracture modes of SLM Ti-6Al-4V. *Materials Science and Engineering: A* **616**, 1-11 (2014).

27. Martin AA, *et al.* Dynamics of pore formation during laser powder bed fusion additive manufacturing. *Nature communications* **10**, 1-10 (2019).
28. Retrived from Polaronyx. <http://www.polaronyx.com/applications.php>.
29. Tuinstra F, Koenig JL. Raman spectrum of graphite. *The Journal of Chemical Physics* **53**, 1126-1130 (1970).
30. Wang Y, Alsmeyer DC, McCreery RL. Raman spectroscopy of carbon materials: structural basis of observed spectra. *Chemistry of Materials* **2**, 557-563 (1990).
31. Sasaki Y, Nishina Y, Sato M, Okamura K. Raman study of SiC fibres made from polycarbosilane. *Journal of Materials Science* **22**, 443-448 (1987).
32. Dennison J, Holtz M, Swain G. Raman spectroscopy of carbon materials. *Spectroscopy* **11**, (1996).
33. Bouillon E, *et al.* Conversion mechanisms of a polycarbosilane precursor into an SiC-based ceramic material. *Journal of Materials Science* **26**, 1333-1345 (1991).
34. Kimoto T, Cooper JA. Appendix C: major physical properties of common SiC polytypes. (2014).
35. Juodkazis S, *et al.* Laser-induced microexplosion confined in the bulk of a sapphire crystal: evidence of multimegabar pressures. *Physical review letters* **96**, 166101 (2006).
36. Knippenberg WF. Growth phenomena in silicon carbide. *Philips Research Report* **18**, 161-274 (1963).

37. Inomata Y, Inoue Z, Mitomo M, Suzuki H. Relation between growth temperature and the structure of SiC crystals grown by the sublimation method. Emmanuel Coll Boston Mass Oriental Science Reseach Library (1969).
38. Gomes de Mesquita Ad. Refinement of the crystal structure of SiC type 6H. *Acta Crystallographica* **23**, 610-617 (1967).
39. Cheng C, Heine V, Needs R. Atomic relaxation in silicon carbide polytypes. *Journal of Physics: Condensed Matter* **2**, 5115 (1990).
40. Bechstedt F, *et al.* Polytypism and properties of silicon carbide. *Physica Status Solidi (b)* **202**, 35-62 (1997).
41. Kirka MM, Nandwana P, Lee Y, Dehoff RR. Solidification and solid-state transformation sciences in metals additive manufacturing. *Scripta Materialia* **135**, 130-134 (2017).
42. Bootsma G, Knippenberg WF, Verspui G. Phase transformations, habit changes and crystal growth in SiC. *Journal of Crystal Growth* **8**, 341-353 (1971).
43. Dolloff RT, Sara R. *Research study to determine the phase equilibrium relations of selected metal carbides at high temperatures.* Aeronautical Systems Division, Air Force Systems Command, US Air Force (1961).
44. Qing J, Richards V, Van Aken DC. Growth stages and hexagonal-rhombohedral structural arrangements in spheroidal graphite observed in ductile iron. *Carbon* **116**, 456-469 (2017).
45. Benedetti M, Fontanari V, Lusuardi D. Effect of graphite morphology on the fatigue and fracture resistance of ferritic ductile cast iron. *Engineering Fracture Mechanics* **206**, 427-441 (2019).

46. Xi J, Liu C, Morgan D, Szlufarska I. An Unexpected Role of H During SiC Corrosion in Water. *The Journal of Physical Chemistry C* **124**, 9394-9400 (2020).
47. Wallace D. Thermodynamics of Crystals John Wiley & Sons. *New York*, (1972).
48. Kern G, Kresse G, Hafner J. Ab initio calculation of the lattice dynamics and phase diagram of boron nitride. *Physical Review B* **59**, 8551 (1999).
49. Liu J, Vohra YK. Raman modes of 6 h polytype of silicon carbide to ultrahigh pressures: A comparison with silicon and diamond. *Physical review letters* **72**, 4105 (1994).
50. del Corro E, de la Roza AO, Taravillo M, Baonza VG. Raman modes and Grüneisen parameters of graphite under compressive biaxial stress. *Carbon* **50**, 4600-4606 (2012).
51. Xi J, Jiang H, Liu C, Morgan D, Szlufarska I. Corrosion of Si, C, and SiC in molten salt. *Corrosion Science* **146**, 1-9 (2019).

Supplementary Files

This is a list of supplementary files associated with this preprint. Click to download.

- [Supplementary.docx](#)